



Article

A Coaxial Triboelectric Fiber Sensor for Human Motion Recognition and Rehabilitation via Machine Learning

Qicheng Ding ^{1,†}, Aamir Rasheed ^{1,†} , Haonan Zhang ^{1,†}, Sara Ajmal ^{1,†}, Ghulam Dastgeer ² , Kamoladdin Saidov ^{3,4}, Olim Ruzimuradov ⁵ , Shavkat Mamatkulov ⁶, Wen He ^{1,*} and Peihong Wang ^{1,*}

¹ School of Materials Science and Engineering, Anhui University, Hefei 230601, China; ms2234098@stu.ahu.edu.cn (Q.D.); aamir786@ahu.edu.cn (A.R.); b21101007@stu.ahu.edu.cn (H.Z.); sara786@ahu.edu.cn (S.A.)

² Department of Physics & Astronomy, Sejong University, Seoul 05006, Republic of Korea; gdstgeer@sejong.ac.kr

³ Department of Electronics and Radio Engineering, Tashkent University of Information Technologies, Tashkent 100084, Uzbekistan; k.saidov@tuit.uz

⁴ Department of Information Technologies, Tashkent International University of Education, Tashkent 100207, Uzbekistan

⁵ Department of Natural and Mathematic Sciences, Turin Polytechnic University in Tashkent, Tashkent 100095, Uzbekistan; o.ruzimuradov@polito.uz

⁶ Institute of Materials Science, Uzbekistan Academy of Sciences, Chingiz Aytmatov 2B St., Tashkent 100084, Uzbekistan; mi-shavkat@yandex.ru

* Correspondence: hewen@ahu.edu.cn (W.H.); wangpeihong2002@ahu.edu.cn (P.W.)

† These authors contributed equally to this work.

Abstract: This work presents the fabrication of a coaxial fiber triboelectric sensor (CFTES) designed for efficient energy harvesting and gesture detection in wearable electronics. The CFTES was fabricated using a facile one-step wet-spinning approach, with PVDF-HFP/CNTs/Carbon black as the conductive electrode and PVDF-HFP/MoS₂ as the triboelectric layer. The incorporation of 1T phase MoS₂ into the PVDF-HFP matrix significantly improves the sensor's output owing to its electron capture capabilities. The sensor's performance was carefully optimized by varying the weight percentage of MoS₂, the thickness of the fiber core, and the CNT ratio. The optimized CFTES, with a core thickness of 156 μm and 0.6 wt% MoS₂, achieved a stable output voltage of ~8.2 V at a frequency of 4 Hz and 10 N applied force, exhibiting remarkable robustness over 3600 s. Furthermore, the CFTES effectively detects human finger gestures, with machine learning algorithms further enhancing its accuracy. This innovative sensor offers a sustainable solution for energy transformation and has promising applications in smart portable power sources and wearable electronic devices.

Keywords: coaxial fiber triboelectric sensor; 1T MoS₂; PVDF-HFP/MoS₂; machine learning; gesture detection



Citation: Ding, Q.; Rasheed, A.; Zhang, H.; Ajmal, S.; Dastgeer, G.; Saidov, K.; Ruzimuradov, O.; Mamatkulov, S.; He, W.; Wang, P. A Coaxial Triboelectric Fiber Sensor for Human Motion Recognition and Rehabilitation via Machine Learning. *Nanoenergy Adv.* **2024**, *4*, 355–366. <https://doi.org/10.3390/nanoenergyadv4040022>

Academic Editors: Dukhyun Choi and Ya Yang

Received: 31 August 2024

Revised: 21 November 2024

Accepted: 25 November 2024

Published: 4 December 2024



Copyright: © 2024 by the authors. Licensee MDPI, Basel, Switzerland. This article is an open access article distributed under the terms and conditions of the Creative Commons Attribution (CC BY) license (<https://creativecommons.org/licenses/by/4.0/>).

1. Introduction

The rapidly increasing prevalence of portable electronics has brought significant innovations to various domains such as smart home automation [1–5], wireless sensor networks [6], healthcare monitoring systems [7,8], artificial intelligence technologies [9–12], human–machine interfaces [13], and the Internet of things [14]. The evolution of these technologies emphasizes the escalating demand for efficient and sustainable power sources [12,13]. Conventional batteries are frequently used in small electronic devices due to their ease of replacement [14]. However, they often fall short in terms of durability and energy efficiency for wearable and wireless devices [12,15]. This limitation underscores the critical demand for power sources that combine sustainability and reliability [16,17]. One approach involves harvesting mechanical energy and converting it into electrical energy using mechanisms such as electromagnetic [18,19], piezoelectric [18,20], and triboelectric [21–23]. Among them,

triboelectric sensors have emerged as a compelling technology due to their effectiveness in transforming mechanical energy into electrical energy through frictional contact between distinct materials, a process known as “triboelectricity” [24–26]. Tribo-electrification is a surface phenomenon and it is mainly dependent on the electrostatic electron exchange between the two surfaces. Most of the frictional coatings utilized in triboelectric applications contain dielectric polymers. Most dielectric polymers are non-conducting in nature, which may affect the electron flow and efficiency of the triboelectric device [27–29]. Coaxial fiber triboelectric sensors (CFTESs) represent a significant technological advancement by combining the triboelectric principle with the structural benefits of fiber-based sensors. The coaxial fiber structure of the triboelectric sensor offers enhanced surface contact area and flexibility, leading to improved charge generation and mechanical durability. This design allows for efficient energy conversion under various deformations, making it highly suitable for wearable and flexible electronics. Additionally, the coaxial configuration enhances sensitivity and stability, contributing to superior TENG performance [30–34].

Motivated by the structural configuration of CFTES, a novel CFTES was introduced by employing a single-step wet-spinning approach. The CFTES features a coaxial configuration in which a central conducting electrode is encapsulated with a triboelectric layer. The conducting electrodes were fabricated using poly (vinylidene fluoride-hexafluoropropylene) (PVDF-HFP) in combination with carbon nanotubes (CNTs) and acetylene black, which possesses good robustness and electrical conductivity. The outer shell of CFTES was prepared using PVDF-HFP and the 1T phase of molybdenum disulfide (1T-MoS₂) as a triboelectric layer. The appreciable mechanical stability, anticorrosive nature, high flexibility, and significant wear and tear resistance of PVDF make it an ideal choice for developing CFTES [35–37]. The 1T-MoS₂, with its high specific surface area, quantum confinement effect, and strong electron-accepting ability, is an ideal candidate for enhancing triboelectric performance. The 1T-MoS₂ phase works as an electron acceptor layer and significantly boosts the sensor’s performance by optimizing the charge transfer efficiency of CFTES [38–41]. The abundant fluorinated functional groups and high tribonegativity in PVDF-HFP and outstanding electron capture capabilities of 1T MoS₂ improve the overall electron affinity and charge density of the triboelectric surface, which leads to high charge accumulation efficiency [42,43].

In this research, we conducted a comprehensive analysis of the fabrication methods, material properties, and performance of a coaxial fiber triboelectric sensor (CFTES) using PVDF-HFP/CNTs/Carbon black and PVDF-HFP/1T-MoS₂. By investigating the impact of material composition, we developed a novel CFTES through a one-step wet-spinning method. The sensor, featuring a PVDF-HFP/CNTs/Carbon black electrode and a PVDF-HFP/1T-MoS₂ triboelectric layer, demonstrated enhanced electron capture due to the inclusion of 1T-MoS₂, significantly improving its output. The CFTES design was optimized by adjusting the MoS₂ content, core thickness, and CNT ratio, resulting in a stable output voltage of ~8 V. The sensor achieved an open-circuit voltage of 8.2 V and a short-circuit current of 74 nA and generated a charge of 2.6 nC with a core diameter of 156 μm and 0.6 wt% MoS₂, exhibiting an optimum sensitivity of 0.79 V/N. Additionally, the sensor’s output was explored under varying tapping frequencies and forces. Beyond these material advancements, machine learning algorithms were integrated to enhance the sensor’s ability to accurately recognize and interpret human finger gestures. This innovation extends the CFTES’s potential applications in interactive and wearable technology, demonstrating its promise in energy harvesting and human-computer interaction

2. Experimental Work

2.1. Chemicals

N,N-Dimethylformamide (DMF), C₃H₇NO, high-purity carbon nanotubes (CNTs), lithium chloride (LiCl), ammonium molybdate (NH₄)₂MoO₄, and urea H₂NCONH₂ were purchased from Aladdin Scientific (Shanghai, China). Polyvinylidene fluoride (PVDF-HFP molecular weight: 40 W) and acetylene black were purchased from Shanghai Aichun

Biotechnology Co., Ltd. (Shanghai, China). Thioacetamide and CH_3CSNH_2 were purchased from Runyou Chemical (Shenzhen, China).

2.2. Synthesis of MoS_2

MoS_2 flakes were prepared using an already reported hydrothermal method with slight modification [44]. Ammonium molybdate tetrahydrate (50 mg), thioacetamide (60 mg), lithium chloride (3.0 g), and urea (200 mg) were mixed in 25 mL of deionized water and continuously stirred for 2 h to ensure complete dissolution. The mixed solution was transferred into a Teflon-lined stainless-steel autoclave and treated in a hydrothermal oven at 180 °C for 18 h. The precipitates were collected via centrifugation and washed multiple times with deionized water and ethanol. The obtained sample was kept for drying in an oven at 60 °C overnight.

2.3. Solution Preparation for Wet Spinning

2.3.1. Preparation of the Outer Layer Solution

Various concentrations of MoS_2 (0 mg, 5 mg, 6 mg, 10 mg, 25 mg, 50 mg, and 75 mg) were initially dispersed in 4 g of DMF solution, and then 1 g of PVDF-HFP was dissolved in 4 g of DMF solution to serve as the spinning solution for the outer friction layer.

2.3.2. Preparation of the Inner Layer Solution

The same mass of CNTs and acetylene black (125 mg, 150 mg, 175 mg, and 200 mg) was dispersed in 9 g of DMF solution, containing 1 g of PVDF-HFP, to obtain the spinning solution for the active electrode.

2.4. Preparation of Coaxial Fibers via Wet Spinning

The inner solution was transferred into a syringe and connected to the inner channel of the spinning needle, while the outer solution was connected to the outer channel of the spinning needle as described above. The injection rates for the inner and outer solutions were $50 \mu\text{L min}^{-1}$ and $100 \mu\text{L min}^{-1}$, respectively. The resulting fibers were immersed in a deionized water coagulation bath for 24 h to remove the DMF, which was displaced by the DI water due to their high miscibility. Finally, the fibers were dried in an oven at 80 °C for 12 h. Overall, the material's cost is USD 0.87 and can be applied at an industrial scale.

2.5. Material Characterization

The samples were observed under an SU1510 scanning electron microscope (SEM) from Hitachi, Japan, to study the microstructure of the surface. We characterized the chemical composition of the sample using X-ray photoelectron spectroscopy.

2.6. Electrical Measurements

All electrical measurements of the fabricated device were performed using a Keithley 6514 electrometer.

3. Results and Discussion

The synthesis scheme for the preparation of the CFTES via the polymer-assisted exfoliation process is schematically depicted in Figure 1. The inner layer is composed of a mixture of PVDF-HFP, CNTs, and acetylene black. In comparison, the outer triboelectric layer consists of PVDF-HFP and 1T- MoS_2 . The morphology of the fabricated composites after wet spinning is depicted in an enlarged section in Figure 1. It can be clearly seen that the CNTs homogeneously covered the surface of PVDF/ MoS_2 and the intact consistent morphology is formed as a result of wet spinning.

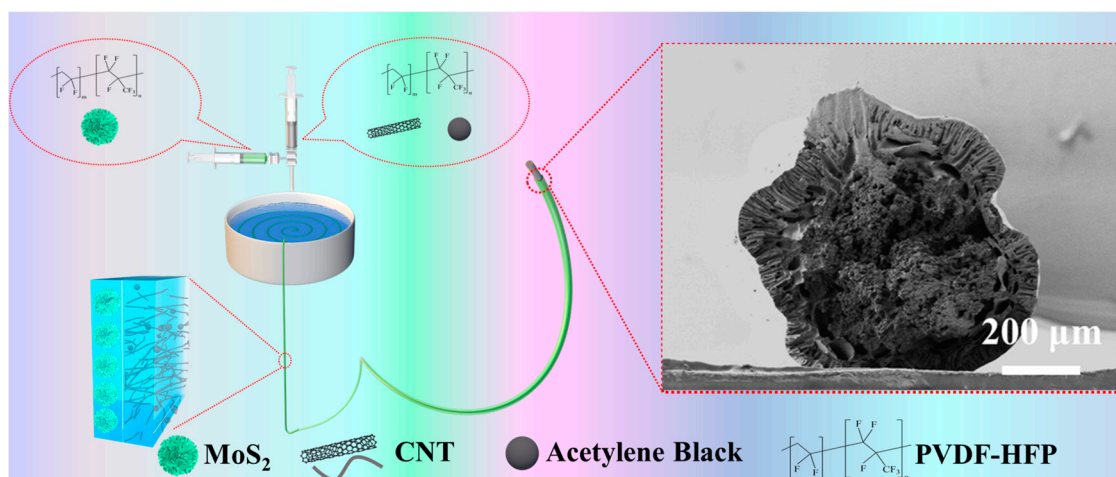


Figure 1. Schematic illustration of the synthesis of the composites via the wet spinning method.

The corresponding EDS mapping in Figure 2a–c further confirms the uniform existence of all corresponding elements C, S, and Mo in the composites. The homogeneity of the fabricated composite fibers can be seen in the scanning electron microscopic (SEM) image in Figure 2d, which clearly confirms the homogeneity of the PVDF matrix and the uniform dispersion of MoS₂ in the composite matrix. The composition of composites was examined using X-ray photoelectron spectroscopy (XPS) data. The wide XPS spectra are given in the supporting data as Figure S1 represents all of the represented elements' peaks of CFTES. The high-resolution XPS of S2p shows the doublet peaks at 162.2 eV and 161.1 eV belonging to S2-2p_{1/2} and 2p_{3/2}. Observation of the peak at 168.2 eV represents the existence of edge sulfur oxidized species (Figure 2e). The high-resolution Mo 3d XPS contains two typical peaks at 228.8 eV and 231.7 eV belonging to Mo 3d_{3/2} and Mo 3d_{5/2} and represents 1T-MoS₂ (Figure 2f). The typical peak at 235.4 eV belongs to the +6 oxidation state of Mo. The Mo oxidation state for 3d_{5/2}, Mo 3d_{3/2} is +4. One more peak at ~225.7 eV is satellite 2 s [45–48]. To further confirm the presence of the 1T phase of MoS₂, X-ray diffraction (XRD) analysis was performed on the sample. The XRD pattern of 1T-MoS₂ exhibited characteristic peaks at approximately 13.5°, 32.6°, and 57.0°, corresponding to the (002), (100), and (110) planes, respectively, as shown in Figure S2. The broad and low-intensity (002) peak, observed at a lower angle than the typical 14.2° for the 2H phase [49,50], indicates the expanded interlayer spacing and confirms the presence of the 1T phase of MoS₂. The synthesized fibers are very elastic, as shown in Figure 2g. Flexibility was confirmed by bending and knotting the fabricated fibers (Figure 2h,i).

The working principle of CFTES is shown in Figure 3. Initially, the triboelectric layer is electrically neutral as it is fully in contact with the external mechanical source. When a mechanical force moves these layers slightly further apart, the phenomenon of contact electrification occurs and the potential difference is induced between the two materials, resulting in a negative charge on the core layer or surface of the fibers. The material is fabricated from the insulating polymers, so the charges persist for a long time on the surface of fibers. This potential difference between the two layers causes the electrons to flow through an external circuit and produce electrical signals. When the layers begin to move closer together, this also induces the potential difference and causes the electronic flow to move in the reverse direction. Once the separation or contact reaches its maximum point, the potential is completely neutralized and the flow of current in the external circuit is stopped. Recompression of the layers via continuous mechanical input in the TENG continuously generates the alternating current.

The electrical performance of the CFTES was assessed by using an external mechanical motor to obtain precise data. The structural features of the materials played a critical role in device output efficiency. Hence, the three influencing parameters including nanofiber thick-

ness, CNT ratio, and the percentage concentration of MoS₂ were systematically optimized, as shown in Figure 4. All of the CFTEs were tested at a tapping frequency of 1 Hz, and open circuit voltage (V_{oc}), short-circuit current (I_{sc}), and charge (Q) were measured. The CFTEs achieves the maximum V_{oc}, I_{sc}, and Q of 580 mV, 5.3 nA, and 0.5 nC, respectively, when the diameter of the external layer is 156 μm (Figure 4a–c). The optical image of various core-shell thicknesses is provided in Supplementary Figure S3. The optimal thickness of 156 μm allowed for maximum charge retention in the nanofibers. By further increasing the thickness, the V_{oc} decreased slightly, whereas the I_{sc} and Q abruptly decreased, making it unsuitable for the CFTEs. The abrupt decline in performance can be attributed to the larger diameters of the fibers, which may enhance charge dissipation and negatively impact charge retention capabilities. Additionally, the increased volume of thicker fibers can lead to higher interfacial resistance between the fiber layers. This increase in resistance, combined with the mechanical stresses introduced by greater thickness, can disrupt the alignment of the triboelectric materials, ultimately resulting in lower current generation and diminished overall performance [51–53]. The optimized 156 μm thickness was tested against the various ratios of m_{CNT}/m_{ACET}. The CFTEs exhibits excellent electrical output performance at an m_{CNT}/m_{ACET} ratio of 125 mg/125 mg, the V_{oc} reaches 570 mV, and the I_{sc} is ~5.8 nA, as shown in Figure 4d,e. Similarly, the highest Q value of ~0.4 nC was examined with the same ratio of 125 mg/125 mg, as shown in Figure 4f.

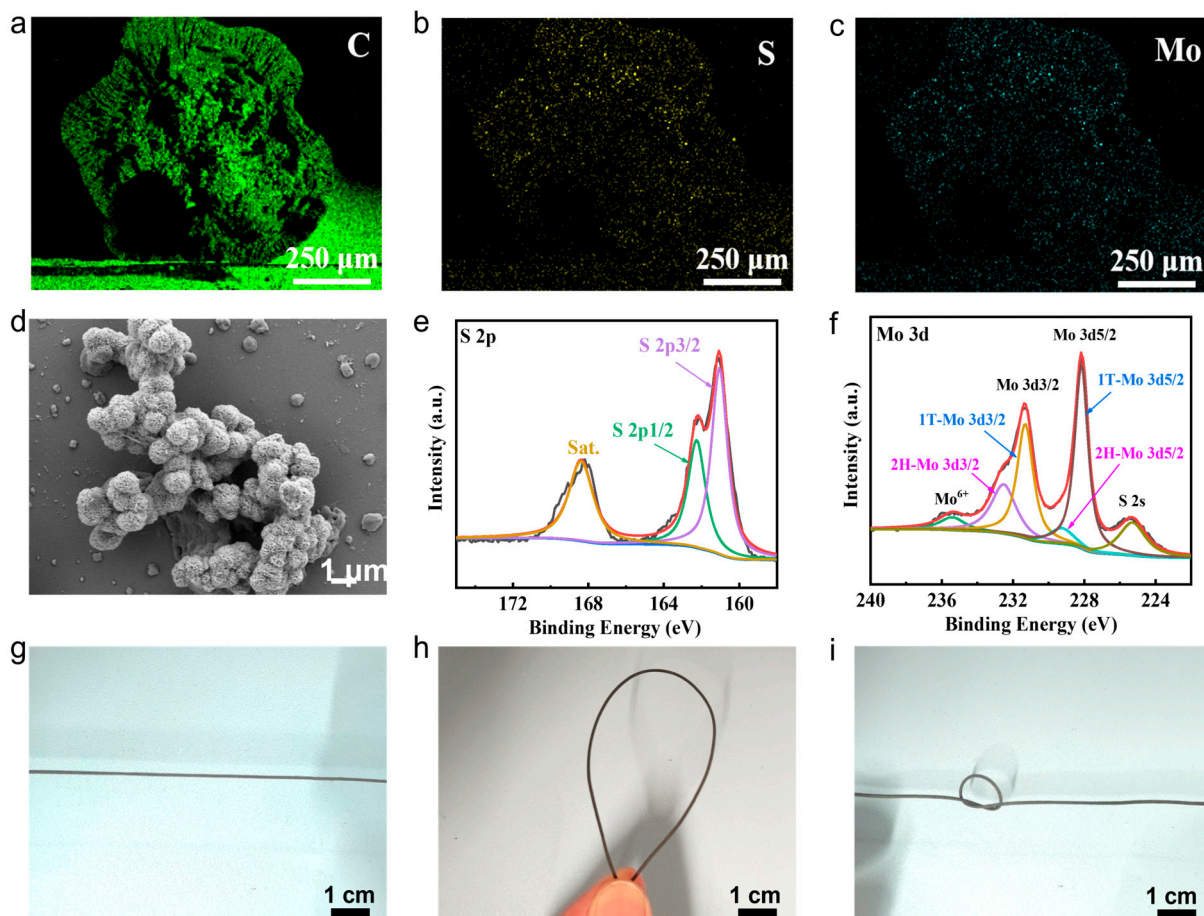


Figure 2. EDS mapping of PVDF-HFP/1T-MoS₂ (a) C, (b) S, (c) and Mo; (d) scanning electron microscopic image of PVDF-HFP/1T-MoS₂; (e) high-resolution S2p XPS spectra of PVDF-HFP/1T-MoS₂; (f) high-resolution Mo3d XPS spectra of PVDF-HFP/1T-MoS₂; (g–i) flexibility test of the fabricated fiber: (g) straight, (h) bending, and (i) knotted.

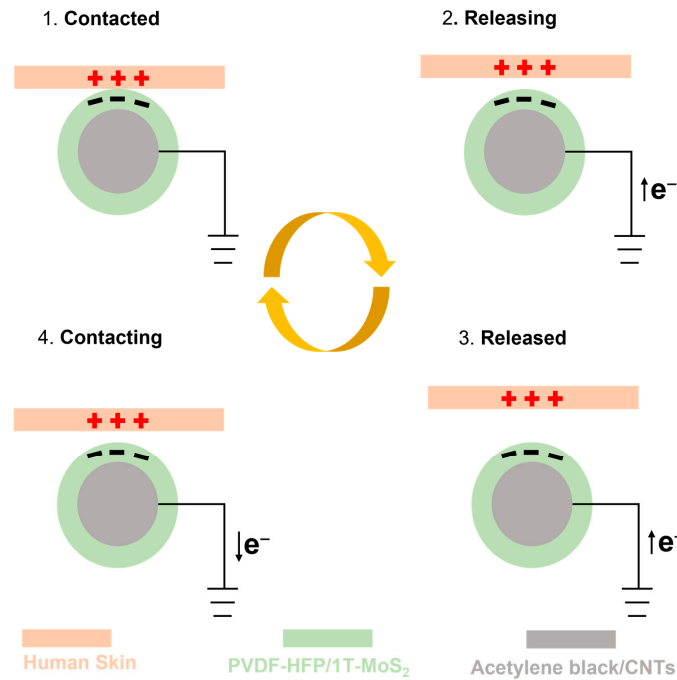


Figure 3. Schematic illustration showing the working principle of the CFTES device.

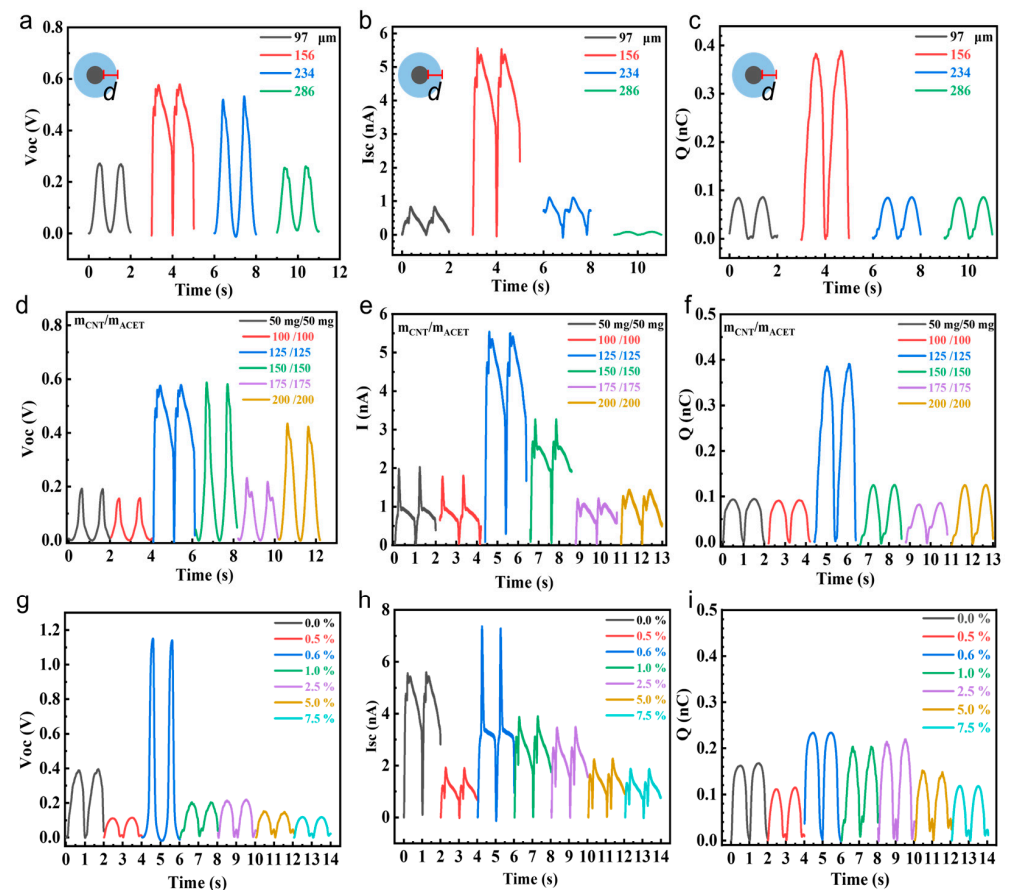


Figure 4. Effect of core diameter on the electrical output performance of the CFTESL (a) output voltage, (b) short-circuit current, and (c) charge; effect of m_{CNT}/m_{ACET} ratio on the electrical output performance of the CFTES: (d) output voltage, (e) short-circuit current, and (f) charge; effect of % of MoS₂ on the electrical output performance of the CFTES: (g) output voltage, (h) short-circuit current, and (i) % of MoS₂.

The triboelectric output of the CFTES gradually increases with the increase in the MoS₂ weight percent (wt%). The maximum improvement in energy harvesting is observed for 0.6 wt% of MoS₂. The output voltage generated by 0.6 wt% of the MoS₂-based CFTES is 2.5 times higher than the undoped MoS₂, as shown in Figure 4d. By further increasing the MoS₂ concentration, Voc in particular tends to be flattened or even reduced. This is due to the fact that a further increase in MoS₂ (wt%) results in an increase in surface contact between MoS₂ and the CNTs. This leads to the form of a conducting network inside the nanofibers, which interferes with the frictional charge transfer, neutralizes some of the charges, and decreases device efficiency [54]. Similarly, the maximum Isc and Q were observed for the 0.6 wt% MoS₂-based CFTES (Figure 4e,f). Hence, the optimal doping concentration of MoS₂ is 0.6 wt%.

The output performance of the CFTES under periodic shocks of various frequencies and applied forces is evaluated in Figure 5. The Voc and Isc under various frequencies are depicted in Figure 5a,b, respectively. The Voc and Isc for the optimized device lie between the frequency range of 1 Hz to 4 Hz in 10 N force. It was observed that both Voc and Isc increase with frequency, indicating the steady achievement of electron flow equilibrium. The value of Q also shows similar trends with respect to frequency as with current, indicating the fast and large amount of charge transfer at higher frequencies. (Figure 5c). A similar trend in Voc and Isc values was observed when increasing the mechanical force from 4 N to 10 N, as depicted in Figure 5d,e. The Q consistently increased with the increase in applied pressure, as shown in Figure 5f. Stability and reliability are critical parameters for evaluating the device's effectiveness. Limitations of the device's life span while operating hinder its practical ability for various applications. Figure 5g illustrates the sensitivity of the fabricated CFTES. The sensor exhibits a sensitivity of approximately 0.23 V/N, which is higher than at increased force levels (~0.79 V/N). This improved sensitivity is likely due to the material's structural integrity being compromised under higher force impacts. Overall, the maximum voltage, current, and transferred charge were found to be 8.2 V, 74 nA, and 2.6 nC, respectively, under optimized conditions. The stability of the as-fabricated TENG device was tested to ensure the mechanical stability of the device at an applied force and frequency of 10 N and 4 Hz, respectively. The stability test in Figure 5h confirms that the CFTES device remains stable under the continuous cycle for 3600 s with no significant difference in the output waveform, validating the reliability of the CFTES. Additionally, we have provided a clear comparison of the performance of our material with already reported works, as shown in Table S1.

The CFTES device was designed for practical implementation to harvest energy from various routine activities. As illustrated in Figure 6, the fabricated CFTES device was mounted on the joints of the five fingers of a human hand. When the device was attached to various fingers and subjected to mechanical force from finger bending during routine activities, it harvested mechanical energy and triggered a voltage signal. Figure 6a shows a real-time 3D graph of the CFTES device while the user bends their fingers at different angles. Continuous cyclic signals were observed during the movement of all five fingers. Figure 6b provides corresponding photographs of the bending motions of the five fingers. The testing technique demonstrated the exceptional sensing capability of the CFTES device, even with low applied force. It also highlights the device's high flexibility, compact bending ability, and ease of transport, making it suitable for practical applications in the future. By collecting data on fibers and processing them using an LSTM model in deep learning, we have successfully developed a method to accurately identify different finger movements. The Voc signals generated by the wearer while performing different finger motions were measured in the experiment. Each finger was measured 220 times and each finger can result in 220 data points. Overall, the resulting dataset with a total of 5 × 220 data points was considered for analysis. The workflow diagram of the LSTM model, along with the confusion matrix of the test set and the finger motion recognition results, is shown in Figure 6c. The method can accurately identify the Voc signals generated by different finger movements, with 92.6% recognition accuracy.

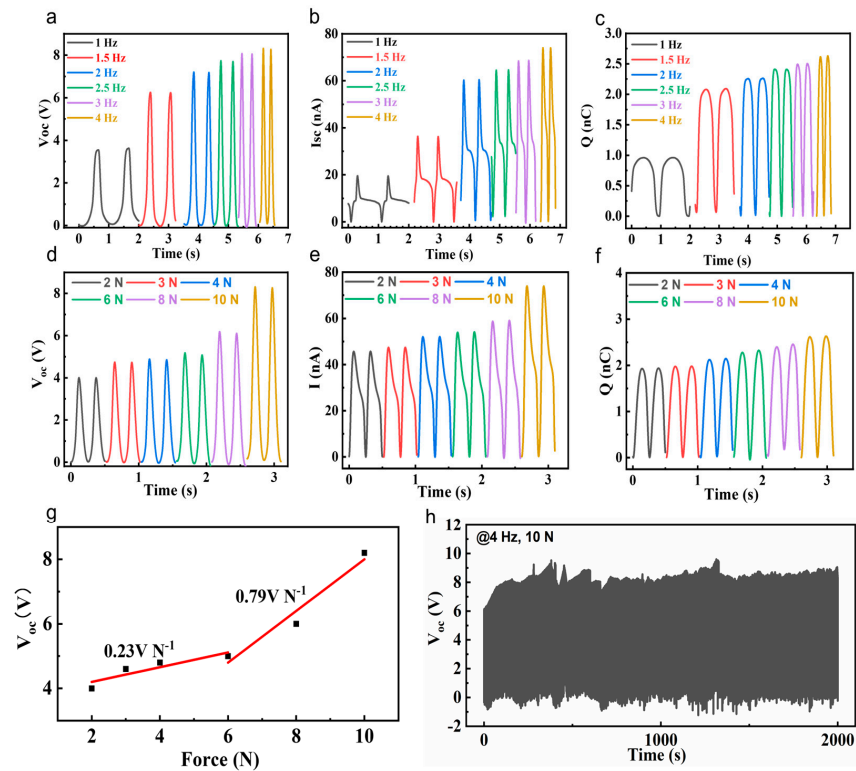


Figure 5. Effect of operating frequency on the electrical properties of the CFTEs: (a) output voltage, (b) short-circuit current, and (c) transferred charge; effect of external force on the electrical properties of the CFTEs: (d) output voltage, (e) short-circuit current, and (f) transferred charge, respectively; (g) sensitivity of the CFTEs and (h) voltage retention of the CFTEs after operation for 3600 s.

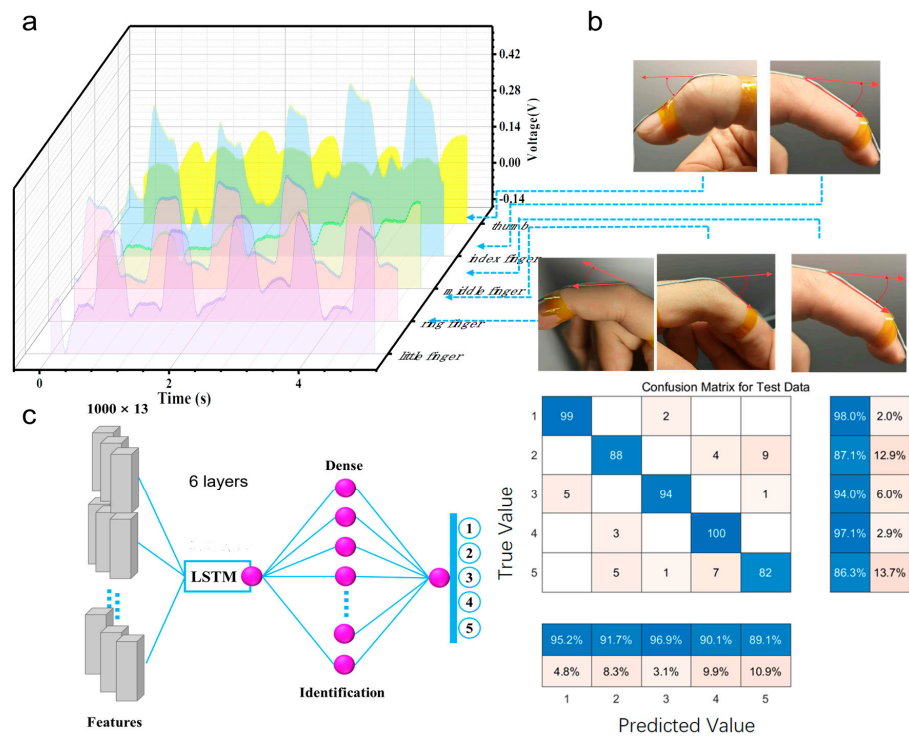


Figure 6. Real-time application of the CFTEs device: (a) 3D graphs for the output voltage generation indicating the bending gestures of human fingers and (b) corresponding images of fingers bending at different angles. (c) Workflow diagram of an LSTM model for deep learning and a confusion matrix for recognizing different finger movements.

4. Conclusions

In summary, we fabricated a highly flexible composite nanofiber material using a wet spinning process, incorporating 1T-MoS₂, CNTs, and PVDF-HFP. The highly flexible nanofibers can generate charge using frictional forces and have been successfully utilized for CFTES devices. The nanofibers are in the tackle and form a core-shell morphology. The device comprises PVDF-HFP/CNTs/Carbon black as its highly efficient conductive electrode, while PVDF-HFP/MoS₂ is an advanced triboelectric layer, ensuring optimal performance and sensitivity. The core/shell morphology synergistically enhances the conductivity as well as the triboelectricity in the CFTES device. The fabricated CFTES device shows cast-improved performance with a PVDF nanofiber thickness of 156 μm, an $m_{\text{CNT}}/m_{\text{ACET}}$ of 125 mg/125 mg, and MoS₂ content of 0.6 wt%, exhibiting the highest electrical output power. Furthermore, the influence of tapping frequency and force on the triboelectric output of the optimized CFTES was also investigated. The results showed that upon raising the tapping frequency, the output performance improved due to fast electron transfer. Similarly, increasing the tapping force resulted in the enhancement of effective area which leads to improved device output performance. The device shows a persistent voltage output of 3600 s, ensuring its high stability. The device can successfully sense human finger movements and the recorded signal was observed, showing its operability in future smart, portable, energy-harvesting, and sensing devices.

Supplementary Materials: The following supporting information can be downloaded at: <https://www.mdpi.com/article/10.3390/nanoenergyadv4040022/s1>. Figure S1. Wide XPS spectra of CFTES nanofibers. Figure S2. XRD pattern of as synthesized MoS₂. Figure S3. The optical image of various core thickness of CFTES nanofibers at the scale bar of 100 μm. Table S1. Performance comparison with previously reported works [55–61].

Author Contributions: Conceptualization, O.R.; Methodology, H.Z. and S.M.; Software, S.A., K.S. and O.R.; Validation, H.Z.; Formal analysis, H.Z. and G.D.; Investigation, Q.D., S.A. and K.S.; Resources, Q.D. and S.M.; Data curation, Q.D. and G.D.; Writing—original draft, A.R.; Writing—review&editing, A.R. and W.H.; Supervision, W.H. and P.W.; Project administration, P.W.; Funding acquisition, W.H. and P.W. All authors have read and agreed to the published version of the manuscript.

Funding: This work was supported by the National Natural Science Foundation of China (52402212), Research start-up funding of Anhui University (S020318031/010, S202418001/077, S202418001/078), Anhui Provincial Natural Science Foundation for Distinguished Young Scholars of China (2208085J16), the Research Fund for the Reserve Candidates of Academic and Technical Leaders in Anhui Province of China (2020H209), the Excellent Research Innovation Team of Anhui Provincial Education Department (2023AH010001), and the State S&T program of Fundamental Investigations of the Academy of Sciences of Republic of Uzbekistan (5921333212).

Data Availability Statement: The original contributions presented in the study are included in the article and Supplementary Material, further inquiries can be directed to the corresponding authors.

Conflicts of Interest: The authors declare that they have no known competing financial interests or personal relationships that could have appeared to have influenced the work reported in this paper.

References

1. Rana, S.S.; Halim, M.A.; Kabir, M.H. Design and implementation of a security improvement framework of Zigbee network for intelligent monitoring in IoT platform. *Appl. Sci.* **2018**, *8*, 2305. [CrossRef]
2. Zou, J.; Zhang, M.; Huang, J.; Bian, J.; Jie, Y.; Willander, M.; Cao, X.; Wang, N.; Wang, Z.L. Coupled supercapacitor and triboelectric nanogenerator boost biomimetic pressure sensor. *Adv. Energy Mater.* **2018**, *8*, 1702671. [CrossRef]
3. Veeramuthu, L.; Cho, C.J.; Venkatesan, M.; Hsu, H.Y.; Zhuo, B.X.; Kau, L.J.; Chung, M.A.; Lee, W.Y.; Kuo, C.C. Muscle fibers inspired electrospun nanostructures reinforced conductive fibers for smart wearable optoelectronics and energy generators. *Nano Energy* **2022**, *101*, 107592. [CrossRef]
4. Kim, S.Y.; Jang, S.; Kim, K.N.; Lee, S.; Chang, H.; Yim, S.; Song, W.; Lee, S.; Lim, J.; Myung, S. Multilayered MoS₂ Sphere-Based Triboelectric–Flexoelectric Nanogenerators as Self-Powered Mechanical Sensors for Human Motion Detection. *ACS Appl. Nano Mater.* **2022**, *5*, 15192–15200. [CrossRef]
5. Ippili, S.; Jella, V.; Thomas, A.M.; Yoon, S.G. The recent progress on halide perovskite-based self-powered sensors enabled by piezoelectric and triboelectric effects. *Nanoenergy Adv.* **2021**, *1*, 3–31. [CrossRef]

6. Tantraviwat, D.; Buarin, P.; Suntalelat, S.; Sripumkhai, W.; Pattamang, P.; Rujjanagul, G.; Inceesungvorn, B. Highly dispersed porous polydimethylsiloxane for boosting power-generating performance of triboelectric nanogenerators. *Nano Energy* **2020**, *67*, 104214. [[CrossRef](#)]
7. Rahman, M.T.; Rana, S.S.; Salaudhin, M.; Maharjan, P.; Bhatta, T.; Park, J.Y. Biomechanical energy-driven hybridized generator as a universal portable power source for smart/wearable electronics. *Adv. Energy Mater.* **2020**, *10*, 1903663. [[CrossRef](#)]
8. Lin, Z.; Chen, J.; Li, X.; Zhou, Z.; Meng, K.; Wei, W.; Yang, J.; Wang, Z.L. Triboelectric nanogenerator enabled body sensor network for self-powered human heart-rate monitoring. *ACS Nano* **2017**, *11*, 8830–8837. [[CrossRef](#)]
9. Dong, K.; Peng, X.; Wang, Z.L. Fiber/fabric-based piezoelectric and triboelectric nanogenerators for flexible/stretchable and wearable electronics and artificial intelligence. *Adv. Mater.* **2020**, *32*, 1902549. [[CrossRef](#)]
10. Chen, T.; Shi, Q.; Zhu, M.; He, T.; Yang, Z.; Liu, H.; Sun, L.; Yang, L.; Lee, C. Intuitive-augmented human-machine multidimensional nano-manipulation terminal using triboelectric stretchable strip sensors based on minimalist design. *Nano Energy* **2019**, *60*, 440–448. [[CrossRef](#)]
11. Maharjan, P.; Bhatta, T.; Cho, H.; Hui, X.; Park, C.; Yoon, S.; Salaudhin, M.; Rahman, M.T.; Rana, S.S.; Park, J.Y. A fully functional universal self-chargeable power module for portable/wearable electronics and self-powered IoT applications. *Adv. Energy Mater.* **2020**, *10*, 2002782. [[CrossRef](#)]
12. Salaudhin, M.; Toyabur, R.; Maharjan, P.; Park, J.Y. High performance human-induced vibration driven hybrid energy harvester for powering portable electronics. *Nano Energy* **2018**, *45*, 236–246. [[CrossRef](#)]
13. Wang, S.; Lin, L.; Xie, Y.; Jing, Q.; Niu, S.; Wang, Z.L. Sliding-triboelectric nanogenerators based on in-plane charge-separation mechanism. *Nano Lett.* **2013**, *13*, 2226–2233. [[CrossRef](#)]
14. Fan, F.R.; Tang, W.; Wang, Z.L. Flexible nanogenerators for energy harvesting and self-powered electronics. *Adv. Mater.* **2016**, *28*, 4283–4305. [[CrossRef](#)]
15. Salaudhin, M.; Park, J.Y. Design and experiment of human hand motion driven electromagnetic energy harvester using dual Halbach magnet array. *Smart Mater. Struct.* **2017**, *26*, 035011. [[CrossRef](#)]
16. Zhu, G.; Lin, Z.-H.; Jing, Q.; Bai, P.; Pan, C.; Yang, Y.; Zhou, Y.; Wang, Z.L. Toward large-scale energy harvesting by a nanoparticle-enhanced triboelectric nanogenerator. *Nano Lett.* **2013**, *13*, 847–853. [[CrossRef](#)]
17. Wang, Z.L.; Chen, J.; Lin, L. Progress in triboelectric nanogenerators as a new energy technology and self-powered sensors. *Energy Environ. Sci.* **2015**, *8*, 2250–2282. [[CrossRef](#)]
18. Mahapatra, S.D.; Mohapatra, P.C.; Aria, A.I.; Christie, G.; Mishra, Y.K.; Hofmann, S.; Thakur, V.K. Piezoelectric materials for energy harvesting and sensing applications: Roadmap for future smart materials. *Adv. Sci.* **2021**, *8*, 2100864. [[CrossRef](#)] [[PubMed](#)]
19. Rana, S.S.; Rahman, M.T.; Salaudhin, M.; Maharjan, P.; Bhatta, T.; Cho, H.; Park, J.Y. A human-machine interactive hybridized biomechanical nanogenerator as a self-sustainable power source for multifunctional smart electronics applications. *Nano Energy* **2020**, *76*, 105025. [[CrossRef](#)]
20. Singh, V.; Meena, D.; Sharma, H.; Trivedi, A.; Singh, B. Investigating the role of chalcogen atom in the piezoelectric performance of PVDF/TMDCs based flexible nanogenerator. *Energy* **2022**, *239*, 122125. [[CrossRef](#)]
21. Singh, H.H.; Khare, N. Flexible ZnO-PVDF/PTFE based piezo-tribo hybrid nanogenerator. *Nano Energy* **2018**, *51*, 216–222. [[CrossRef](#)]
22. Singh, H.H.; Khare, N. Improved performance of ferroelectric nanocomposite flexible film based triboelectric nanogenerator by controlling surface morphology, polarizability, and hydrophobicity. *Energy* **2019**, *178*, 765–771. [[CrossRef](#)]
23. Rahman, M.T.; Salaudhin, M.; Maharjan, P.; Rasel, M.; Cho, H.; Park, J.Y. Natural wind-driven ultra-compact and highly efficient hybridized nanogenerator for self-sustained wireless environmental monitoring system. *Nano Energy* **2019**, *57*, 256–268. [[CrossRef](#)]
24. Yu, B.; Yu, H.; Huang, T.; Wang, H.; Zhu, M. A biomimetic nanofiber-based triboelectric nanogenerator with an ultrahigh transfer charge density. *Nano Energy* **2018**, *48*, 464–470. [[CrossRef](#)]
25. Jiang, H.; Lei, H.; Wen, Z.; Shi, J.; Bao, D.; Chen, C.; Jiang, J.; Guan, Q.; Sun, X.; Lee, S.-T. Charge-trapping-blocking layer for enhanced triboelectric nanogenerators. *Nano Energy* **2020**, *75*, 105011. [[CrossRef](#)]
26. Han, J.; Yang, X.; Liao, L.; Zhou, G.; Wang, G.; Xu, C.; Hu, W.; Debora, M.E.R.; Song, Q. Photoinduced triboelectric polarity reversal and enhancement of a new metal/semiconductor triboelectric nanogenerator. *Nano Energy* **2019**, *58*, 331–337. [[CrossRef](#)]
27. Chen, J.; Guo, H.; He, X.; Liu, G.; Xi, Y.; Shi, H.; Hu, C. Enhancing performance of triboelectric nanogenerator by filling high dielectric nanoparticles into sponge PDMS film. *ACS Appl. Mater. Interfaces* **2016**, *8*, 736–744. [[CrossRef](#)] [[PubMed](#)]
28. Huang, C.; Lu, G.; Zhang, Y.; Zhu, K.; Cui, S.; Chen, W.; Wu, Z.; Qiu, M.; Mi, L. Programmable triboelectric nanogenerators dependent on the secondary building units in cadmium coordination polymers. *Inorg. Chem.* **2020**, *60*, 550–554. [[CrossRef](#)]
29. Khandelwal, G.; Chandrasekhar, A.; Maria Joseph Raj, N.P.; Kim, S.J. Metal-organic framework: A novel material for triboelectric nanogenerator-based self-powered sensors and systems. *Adv. Energy Mater.* **2019**, *9*, 1803581. [[CrossRef](#)]
30. Yu, X.; Pan, J.; Zhang, J.; Sun, H.; He, S.; Qiu, L.; Lou, H.; Sun, X.; Peng, H. A coaxial triboelectric nanogenerator fiber for energy harvesting and sensing under deformation. *J. Mater. Chem. A* **2017**, *5*, 6032–6037. [[CrossRef](#)]
31. Jiang, F.; Zhou, X.; Lee, P.S. Fiber-and Textile-Based Triboelectric Nanogenerators. In *Handbook of Triboelectric Nanogenerators*; Springer: Cham, Switzerland, 2023; pp. 1–39.
32. Niu, L.; Miao, X.; Jiang, G.; Wan, A.; Li, Y.; Liu, Q. Biomechanical energy harvest based on textiles used in self-powering clothing. *J. Eng. Fibers Fabr.* **2020**, *15*, 1558925020967352. [[CrossRef](#)]

33. Lin, S.; Yang, W.; Zhu, X.; Lan, Y.; Li, K.; Zhang, Q.; Li, Y.; Hou, C.; Wang, H. Triboelectric micro-flexure-sensitive fiber electronics. *Nat. Commun.* **2024**, *15*, 2374. [[CrossRef](#)] [[PubMed](#)]
34. Yu, B.; Yu, H.; Wang, H.; Zhang, Q.; Zhu, M. High-power triboelectric nanogenerator prepared from electrospun mats with spongy parenchyma-like structure. *Nano Energy* **2017**, *34*, 69–75. [[CrossRef](#)]
35. Shi, L.; Jin, H.; Dong, S.; Huang, S.; Kuang, H.; Xu, H.; Chen, J.; Xuan, W.; Zhang, S.; Li, S. High-performance triboelectric nanogenerator based on electrospun PVDF-graphene nanosheet composite nanofibers for energy harvesting. *Nano Energy* **2021**, *80*, 105599. [[CrossRef](#)]
36. Pu, X.; Zha, J.-W.; Zhao, C.-L.; Gong, S.-B.; Gao, J.-F.; Li, R.K. Flexible PVDF/nylon-11 electrospun fibrous membranes with aligned ZnO nanowires as potential triboelectric nanogenerators. *Chem. Eng. J.* **2020**, *398*, 125526. [[CrossRef](#)]
37. Shen, Y.; Lua, A.C. Preparation and characterization of mixed matrix membranes based on PVDF and three inorganic fillers (fumed nonporous silica, zeolite 4A and mesoporous MCM-41) for gas separation. *Chem. Eng. J.* **2012**, *192*, 201–210. [[CrossRef](#)]
38. Xue, F.; Chen, L.; Wang, L.; Pang, Y.; Chen, J.; Zhang, C.; Wang, Z.L. MoS₂ tribotronic transistor for smart tactile switch. *Adv. Funct. Mater.* **2016**, *26*, 2104–2109. [[CrossRef](#)]
39. Wu, C.; Kim, T.W.; Park, J.H.; An, H.; Shao, J.; Chen, X.; Wang, Z.L. Enhanced triboelectric nanogenerators based on MoS₂ monolayer nanocomposites acting as electron-acceptor layers. *ACS Nano* **2017**, *11*, 8356–8363. [[CrossRef](#)] [[PubMed](#)]
40. Zhang, Y.; Zeng, W.; Li, Y. The hydrothermal synthesis of 3D hierarchical porous MoS₂ microspheres assembled by nanosheets with excellent gas sensing properties. *J. Alloys Compd.* **2018**, *749*, 355–362. [[CrossRef](#)]
41. Hedau, B.; Kang, B.-C.; Ha, T.-J. Enhanced triboelectric effects of self-poled MoS₂-embedded PVDF hybrid nanocomposite films for bar-printed wearable triboelectric nanogenerators. *ACS Nano* **2022**, *16*, 18355–18365. [[CrossRef](#)]
42. Chen, X.; Han, X.; Shen, Q.D. PVDF-based ferroelectric polymers in modern flexible electronics. *Adv. Electron. Mater.* **2017**, *3*, 1600460. [[CrossRef](#)]
43. Lee, J.P.; Lee, J.W.; Baik, J.M. The progress of PVDF as a functional material for triboelectric nanogenerators and self-powered sensors. *Micromachines* **2018**, *9*, 532. [[CrossRef](#)] [[PubMed](#)]
44. Bo, Z.; Cheng, X.; Yang, H.; Guo, X.; Yan, J.; Cen, K.; Han, Z.; Dai, L. Ultrathick MoS₂ films with exceptionally high volumetric capacitance. *Adv. Energy Mater.* **2022**, *12*, 2103394. [[CrossRef](#)]
45. Vilian, A.E.; Ranjith, K.S.; Hwang, S.K.; Bhaskaran, G.; Alhamadi, M.; Park, S.Y.; Huh, Y.S.; Han, Y.-K. Interface engineering of MoS₂ nanopetal grown on carbon nanofibers for the electrocatalytic sensing of mercury (II) and efficient hydrogen evolution. *Mater. Today Nano* **2022**, *20*, 100262. [[CrossRef](#)]
46. Wu, M.; Zhan, J.; Wu, K.; Li, Z.; Wang, L.; Geng, B.; Wang, L.; Pan, D. Metallic 1T MoS₂ nanosheet arrays vertically grown on activated carbon fiber cloth for enhanced Li-ion storage performance. *J. Mater. Chem. A* **2017**, *5*, 14061–14069. [[CrossRef](#)]
47. Mohana Rani, G.; Ranjith, K.S.; Ghoreishian, S.M.; Vilian, A.E.; Roh, C.; Umaphathi, R.; Han, Y.-K.; Huh, Y.S. Fabrication of MoS₂ Petals-Decorated PAN Fibers-Based Triboelectric Nanogenerator for Energy Harvesting and Smart Study Room Touch Sensor Applications. *Adv. Fiber Mater.* **2024**, *6*, 1825–1838. [[CrossRef](#)]
48. Sarma, S.; Ray, S.C. Trigonal (1T) and hexagonal (2H) mixed phases MoS₂ thin films. *Appl. Surf. Sci.* **2019**, *474*, 227–231. [[CrossRef](#)]
49. Zhang, Z.; Dong, Y.; Liu, G.; Li, J.; Sun, H.; Luo, H.; Liu, S. The ultrafine monolayer 1 T/2H-MoS₂: Preparation, characterization and amazing photocatalytic characteristics. *Colloids Surf. A Physicochem. Eng. Asp.* **2020**, *589*, 124431. [[CrossRef](#)]
50. Li, Z.; Han, M.; Zhang, Y.; Yuan, F.; Fu, Y.; Yu, J. Single-Layered MoS₂ Fabricated by Charge-Driven Interlayer Expansion for Superior Lithium/Sodium/Potassium-Ion-Battery Anodes. *Adv. Sci.* **2023**, *10*, 2207234. [[CrossRef](#)]
51. Huang, T.; Lu, M.; Yu, H.; Zhang, Q.; Wang, H.; Zhu, M. Enhanced power output of a triboelectric nanogenerator composed of electrospun nanofiber mats doped with graphene oxide. *Sci. Rep.* **2015**, *5*, 13942. [[CrossRef](#)]
52. Zhang, W.; Sun, Q.; Shen, Z.; Liu, J.; Wang, X. Effect of Diameter on the Structural Evolution and Tensile Properties of Electrospun PAN-Based Carbon Nanofiber Mats. *ACS Omega* **2023**, *8*, 19002–19005. [[CrossRef](#)] [[PubMed](#)]
53. Alshahrani, A.; Kulasegaram, S. Effect of fibre diameter and tensile strength on the mechanical, fracture, and fibre distribution properties of eco-friendly high-strength self-compacting concrete. *Constr. Build. Mater.* **2023**, *403*, 133161. [[CrossRef](#)]
54. Sun, C.; Zu, G.; Wei, Y.; Song, X.; Yang, X. Flexible triboelectric nanogenerators based on electrospun poly(vinylidene fluoride) with MoS₂/carbon nanotube composite nanofibers. *Langmuir* **2022**, *38*, 1479–1487. [[CrossRef](#)] [[PubMed](#)]
55. Feng, C.; Cai, L.; Zhu, G.; Chen, L.; Xie, X.; Guo, J. Nanocellulose and multi-walled carbon nanotubes reinforced polyacrylamide/sodium alginate conductive hydrogel as flexible sensor. *J. Colloid Interface Sci.* **2024**, *677*, 692–703. [[CrossRef](#)]
56. Zhou, L.; Liu, X.; Zhong, W.; Pan, Q.; Sun, C.; Gu, Z.; Fang, J.; Li, C.; Wang, J.; Dong, X.; et al. Wearable Smart Silicone Belt for Human Motion Monitoring and Power Generation. *Polymers* **2024**, *16*, 2146. [[CrossRef](#)]
57. Tao, R.; Mao, Y.; Gu, C.; Hu, W. Integrating all-yarn-based triboelectric nanogenerator/supercapacitor for energy harvesting, storage and sensing. *Chem. Eng. J.* **2024**, *496*, 154358. [[CrossRef](#)]
58. Zhang, J.; Ma, C.; Hao, Y.; Chen, W. A flexible triboelectric nanogenerator based on TiO₂ nanoarrays and polyoxometalate for harvesting biomechanical energy. *ACS Appl. Nano Mater.* **2024**, *7*, 16922–16931. [[CrossRef](#)]
59. Ding, X.; Cao, H.; Zhang, X.; Li, M.; Liu, Y. Large Scale Triboelectric Nanogenerator and Self-Powered Flexible Sensor for Human Sleep Monitoring. *Sensors* **2018**, *18*, 1713. [[CrossRef](#)]

60. Liu, B.; Xie, Z.; Feng, Q.; Wang, Y.; Zhang, M.; Lu, Z.; Mao, Y.; Zhang, S. Biodegradable flexible triboelectric nanogenerator for winter sports monitoring. *Front. Mater.* **2024**, *11*, 1400258. [[CrossRef](#)]
61. Duan, Z.; Ge, N.; Hong-Kwan, C.; Sin-Young, S. A pipe arrangement structure triboelectric nanogenerator for mechanical energy harvesting and sports training monitoring. *APL Mater.* **2024**, *12*, 031134. [[CrossRef](#)]

Disclaimer/Publisher's Note: The statements, opinions and data contained in all publications are solely those of the individual author(s) and contributor(s) and not of MDPI and/or the editor(s). MDPI and/or the editor(s) disclaim responsibility for any injury to people or property resulting from any ideas, methods, instructions or products referred to in the content.